J Mater Sci (2011) 46:6131–6139
DOI 10.1007/s10853-011-5578-5

Fracture analysis of ceramic femoral head in hip arthroplasty based on microdamage monitoring using acoustic emission

Yukiya Yamada · Shuichi Wakayama · Junji Ikeda · Fumiaki Miyaji

Received: 17 February 2011 / Accepted: 19 April 2011 / Published online: 3 May 2011

Abstract Damage accumulation during compression testing of the alumina femoral head used in hip arthroplasty was monitored using an acoustic emission (AE) technique. Because a number of mechanical noises due to friction disturbed the AE measurement during the test using a conventional testing configuration standardized in ISO 7206, the testing apparatus was modified so that AE signals from microdamage were detected successfully. During the compression tests of femoral heads, a rapid increase in AE energy was observed before the final fracture. Dye penetration observations demonstrated that the rapid increase in AE energy correlated with the formation of maincrack which leads to the final fracture. The stress distribution in femoral heads was analyzed using finite element analysis (FEA). The critical stress for maincrack formation and the final fracture strength were determined. Finally, fundamental insights into the development of a technique for assessing the long-term reliability of ceramic femoral heads were obtained.

Introduction

Ceramics, such as alumina or zirconia, have been used for implants, including femoral heads in hip arthroplasty, because of their excellent biocompatibility [1, 2]. The design lifetime of these ceramic components is 10–15 years. However, it has been reported that more than a half of some lots have broken in vivo within a few years of surgery [3]. Considering the quality of life of patients, the long-term reliability of ceramic implants is extremely important.

Several approaches for assessing the reliability of structural ceramics have been reported [4–9]. In the early 1970s, Evans [4] described the subcritical crack growth behavior in ceramics and proposed a method of lifetime prediction according to the single crack growth law: the stress intensity-crack growth rate (K-v) relationship. Fuller et al. [9] applied the K-v concept to the lifetime prediction after proof testing of ceramic components. In their analyses, the macroscopic subcritical growth of a single crack from a pre-existing flaw was assumed, although it is an oversimplification of the practical fracture process in ceramic components. It should be pointed out that the characterization of microfracture process is required.

Recently, proof testing of ceramic femoral heads was investigated and an improved test technique was reported [10]. However, there may be still weak components in surviving implants that sustain damage during the proof test. A sophisticated technique to detect microdamage during testing is required.

From these perspectives, the authors investigated the microfracture process during bending tests of alumina ceramics, including medical-grade alumina used for implants, using an acoustic emission (AE) technique [11–13]. It was found that the AE energy increased rapidly before the final fracture. Based on the AE source locations and observations of the fracture process using a fluorescent dye penetration technique, it was found that the AE activity could be attributed to formation of the maincrack. It was then demonstrated that the microfracture process during the

Y. Yamada · S. Wakayama (✉)
Graduate Student of Mechanical Engineering, Tokyo Metropolitan University, 1-1 Minami-Ohsawa, Hachioji, Tokyo 192-0397, Japan
e-mail: wakayama@tmu.ac.jp

J. Ikeda · F. Miyaji
Japan Medical Materials Co, Uemura Nissei Bldg. 9F, 3-3-31, Miyahara, Yodogawa, Osaka 532-0003, Japan

bending test of alumina consists of the accumulation of microdamage, followed by formation of the maincrack, which grows to the final fracture. The critical stress for maincrack formation was determined as the stress at the point when the AE signals increased rapidly. The final fracture was found to be sensitive to initiation of the maincrack, suggesting that an evaluation of critical stress is essential for assessing the reliability of bioceramics. Furthermore, the authors demonstrated that weak components damaged during proof tests can be removed based on AE monitoring of microdamage [13]. However, ceramic components, such as femoral heads, are subjected to a more complex stress state when they are implanted, while the bending specimens are subjected to uniaxial stress.

In this article, compression tests of alumina femoral heads used in hip arthroplasty and AE monitoring of microdamage were carried out. The objectives of the article are to develop a non-destructive technique for monitoring microdamage during compression fracture of a ceramic femoral head and to obtain fundamental knowledge for developing a technique for assessing long-term reliability such as proof testing of ceramic femoral heads. To measure the AE signals from microdamage in femoral heads, the testing apparatus was modified. The microdamage that occurred during the compression tests was monitored using an AE technique and the microfracture process was analyzed. In addition, the stress distribution in the femoral head was calculated using finite element analysis (FEA).

Experimental procedure

Specimen

The specimens tested in this study were femoral heads with a diameter of 22.2 mm made from high-purity alumina (BIOCERAM, Japan Medical Materials Co.). A picture of a specimen is shown in Fig. 1. The material and mechanical properties of alumina are summarized in Table 1. All of the specimens were washed in acetone in an ultrasonic bath for 30 min and dried in a vacuum oven for 2 h at 150 °C.

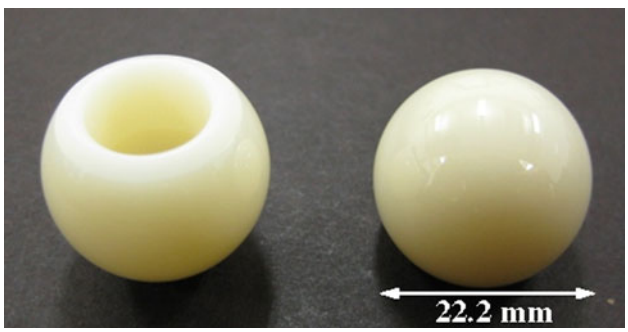

Fig. 1 Picture of a specimen. The material is medical-grade alumina and the diameter of the specimen is 22.2 mm. The material and mechanical properties are summarized in Table 1

Table 1 Material and mechanical properties of the specimen

Density (g/cm^3)	Purity (%)	Average grain size (μm)	Young's modulus (GPa)	Poisson's ratio (−)
3.97	>99.9	1.4	400	0.24

Testing configurations

In this article, testing configuration, which enables the AE measurement during the compression tests of femoral heads. Figure 2a illustrates the testing apparatus standardized in ISO7206 [14]. As the figure shows, a conical loading rod is inserted into the bore of femoral heads, in which the lower part is supported by an annealed copper ring, and the bore is then expanded. The mouth of the bore is subjected to the maximum hoop stress. The strong friction between the loading rod and material is predicted to cause a large amount of mechanical noise, which affects the AE measurement, as described below (Fig. 6).

Thus, a modified testing apparatus was developed, in which the frictional noise was reduced considerably, enabling us to monitor microdamage by limiting the relative sliding. Figure 2b illustrates the modified apparatus. The concept of this system is derived from the Ring Burst

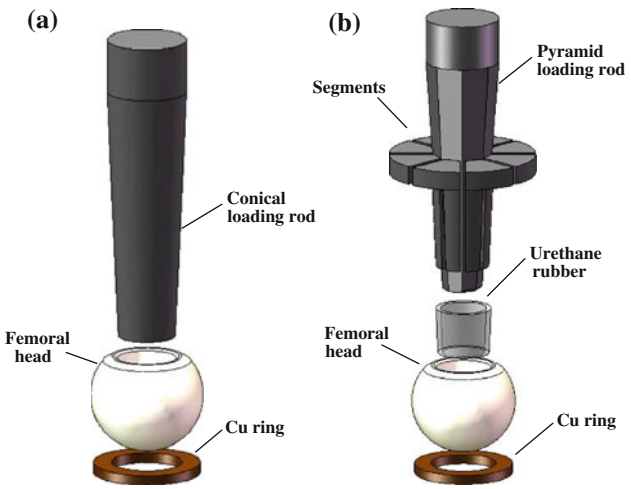

Fig. 2 Schematic illustration of the testing apparatus. **a** The testing apparatus standardized in ISO 7206. Stress was applied to the specimen by compressing the loading rod. Strong friction between the rod and material caused a large amount of mechanical noise, which affected the AE measurement. **b** Modified testing apparatus. A pyramidal rod was inserted into the divided segments so that segments were expanded in the radial direction. The radial load was applied to the specimen through urethane rubber. The frictional noise was reduced by limiting the relative sliding

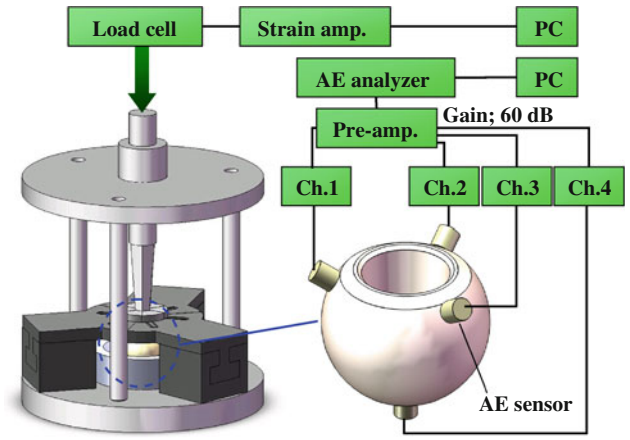

Fig. 3 Schematic diagram of the testing configuration (modified apparatus). AE signals were monitored using four-channel AE sensors with a resonant frequency of 450 kHz. The total gain was 60 dB and the threshold level was ~18 μV at the input of pre-amplifiers. The difference in arrival times between sensors was used to locate the AE sources

Test developed for filament wound pressure vessels made from fiber-reinforced plastics [15, 16]. In this system, a pyramidal loading rod is inserted into the divided segments so that segments are expanded in the radial direction. Similarly to the conventional apparatus, a radial load was applied to the specimen via urethane rubber, which avoided stress concentration.

The friction between the loading rod and segments was minimized by coating the contacting surfaces of the parts with a dry-type fluorine lubricant before inserting the assembled segments into the bore of the femoral head. Furthermore, by constraining the vertical movement of the segments, the relative sliding and friction between the segments and specimen can be minimized. These enabled the detection of AE signals from microcracking, as demonstrated below.

Compression tests and AE measurement

A schematic diagram of the measuring system is shown in Fig. 3. Compression tests were carried out in air at room temperature under a constant loading rate of 0.5 mm/min. During the compression test, the AE signals were monitored by four-channel AE sensors attached to the surface of the specimen using cyanoacrylate adhesive, and recorded with an AE analyzer (MISTRAS, Physical Acoustic). Piezoelectric elements (PZT) with a diameter of 3 mm and height of 3 mm (Z3T3D-LYX C6, Fuji Ceramics) were used as the AE sensors. Then, the sensitivity was calibrated carefully using the pencil lead break as a simulated AE source (Hsu-Nielsen source) before each test. The resonant frequency of the sensors was 450 kHz. The total gain was 60 dB and the threshold level was ~18 μV at the input level of the pre-amplifiers. The sampling rate was 8 MHz and a bandpass filter with a range of 200–1200 kHz was used. The AE energy (time-integral over the voltage signal squared) was used as a measure of damage severity in the fracture analysis.

The AE source location was also calculated using the longitudinal wave velocity of the material and the difference in arrival times between the AE channels. The wave velocity was measured using an ultrasonic pulse and determined to be 10,000 m/s in a preliminary experiment. The arrival times of the AE signal were determined directly from each recorded waveform. In this study, there were four channels, which satisfies the minimum requirement for the three-dimensional location of the AE sources. However, only three of the four channel signals were available for calculating the AE source location, because the bore interfered with the acoustic wave propagation from one channel. Thus, the authors assumed that the nucleation sites of microcracks were on the inner wall of the bore, consistent with the experimental result (Fig. 10). A table of the source locations and corresponding differences in arrival times was constructed by calculating the travelling time of AE signals from the longitudinal wave velocity and the distance between the assumed AE source and sensors before the tests. Then, the source location was determined by comparing the experimental data with the table. The error in the source location was ~1 mm, which was verified in a preliminary experiment using a simulated AE source (Hsu-Nielsen source).

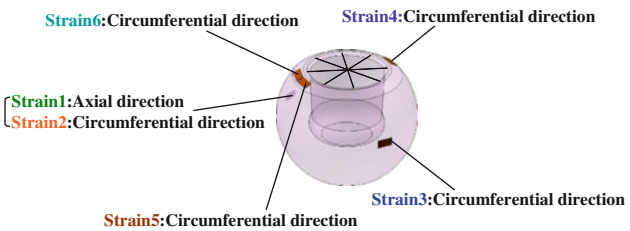

Fig. 4 Location of the strain measurement. Three gauges were attached on the great circle and another three gauges were placed close to the mouth of the bore. The measurement locations were chosen to investigate the effect of divided segments (*Strains 1, 2,* and *6*: segment boundaries, *Strains 3, 4,* and *5*: middle of the segments)

Experimental results

Comparison of the strain distribution

The mechanical strain during the compression test was measured by strain gauges to verify the stress distribution in the femoral heads tested using the conventional and modified testing configurations. The locations and directions of the strain gauges are shown in Fig. 4. Three gauges were attached on the great circle of the specimen and

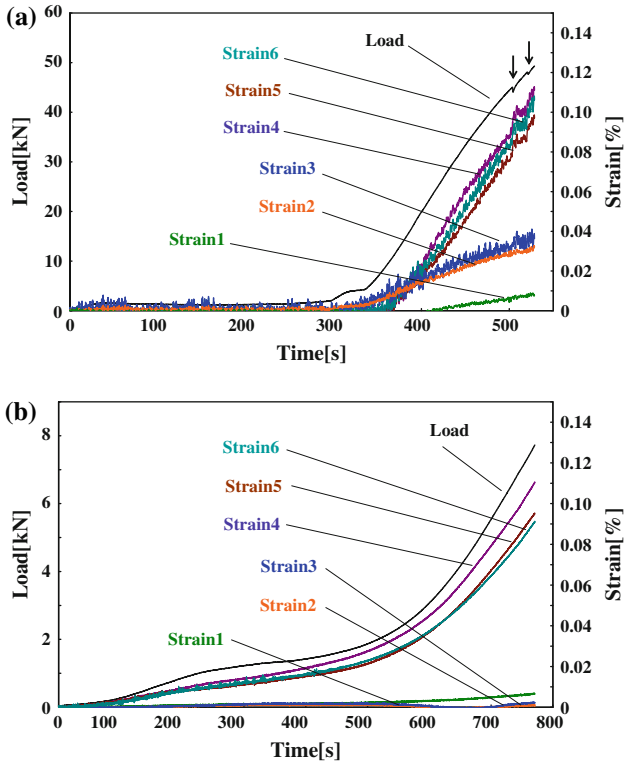

Fig. 5 Results of the strain measurement. **a** Result using the conventional apparatus. The strain at the mouth of bore, where the final fracture initiates, was greater than that on the great circle. There were small decreases in the load (*arrows*) that reflect the stick–slip movement of the loading rod. **b** Result using the modified apparatus. Considering the equivalence of *strains 5* and *6*, the stress concentration at the segment boundary was restrained by the urethane rubber. For the modified apparatus, the load at fracture was reduced by ~1/10 because the friction was reduced

another three gauges were placed close to the mouth of the bore.

The results of load and strain measurements are shown in Fig. 5a and b for the conventional and modified testing apparatus, respectively. Fluctuation in the strains due to electromagnetic noise is recognized in Fig. 5a, but it did not affect the comparison of strain behaviors between the two types of testing apparatus. As seen in Fig. 5b, the load increases smoothly and monotonically in the modified apparatus, while small drops in load (indicated by arrows) are seen in Fig. 5a, reflecting the stick–slip movement of the loading rod in the conventional apparatus.

Strains 1, 2, and 3 (great circle) are larger with the conventional apparatus than the modified apparatus. The influence of these differences on the fracture behavior is negligible because the fracture of the femoral ball was initiated from the region around the mouth of the bore. On the other hand, Strains 4, 5, and 6 (mouth of the bore) are larger than those on the great circle. The difference in Strains 4, 5, and 6 for both apparatuses suggests misalignment of the loading rod and specimen, indicating the need for careful set-up. However, the stress concentration at the boundary of the segments in the modified apparatus was restrained successfully using urethane rubber, because Strains 5 and 6 are equivalent (Fig. 5b).

The maximum strains at the fracture of femoral ball were almost same (~0.12) for both apparatuses. Furthermore, the tendencies of the strain behaviors were quite similar to each other. Consequently, it can be concluded that the deformation behavior in the femoral heads was essentially the same for both apparatus. It is worth noting that the load at fracture for the modified apparatus was reduced considerably (~1/10) because the friction between components was minimized.

AE behavior during compression tests

The results of the AE measurements during the compression test of a femoral head using the conventional apparatus are shown in Fig. 6. As the figure shows, the cumulative AE energy increased linearly, which resulted from the limitation of the detecting rate of the AE measurement system. The source of these AE signals must be mechanical noise due to the friction between the loading rod and specimen. The figure suggests that most of the AE signals from microdamage were lost during the dead-time in the acquisition of noise signals. Consequently, it was concluded that the AE monitoring of microdamage in a specimen is impossible in tests using the conventional apparatus.

Figure 7 shows (a) the load and cumulative AE energy, and (b) AE source location during the compression test using the modified apparatus. An intermittent increase in the AE energy was observed during the test and the AE energy increased rapidly at ~700 s. Simultaneously, relatively large amplitude AE signals were detected at the site of fracture origin (Fig. 7b). The subsequent large signals

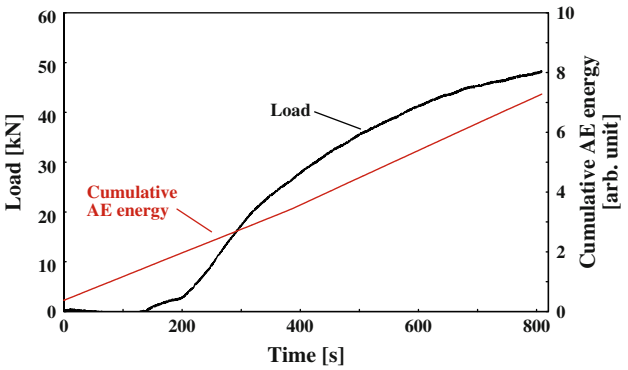

Fig. 6 AE behavior during the compression test using the conventional apparatus. The AE signals were correlated with the mechanical noise due to friction between the loading rod and specimen. The AE monitoring of microdamage would be impossible in tests using the conventional apparatus

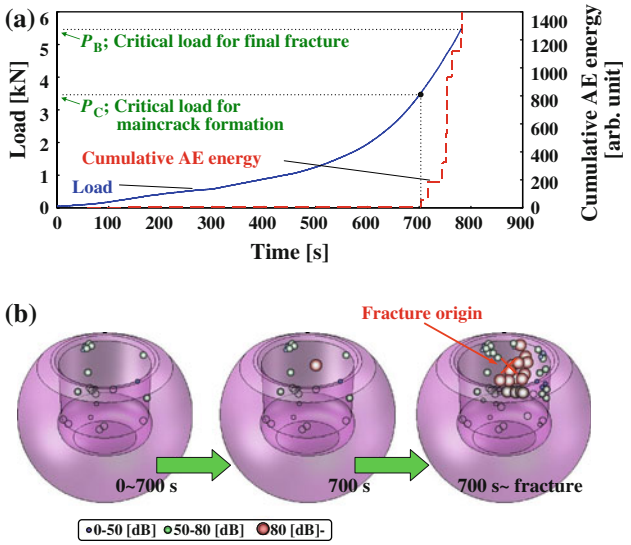

Fig. 7 Typical result of the compression test using the modified apparatus. **a** The load and cumulative AE energy. An intermittent increase in the AE energy was observed. A rapid increase in the AE energy was observed at ~700 s. **b** AE source location. When the cumulative AE energy increased rapidly (~700 s), a relatively large signal was detected on the inner wall at the site of fracture initiation. The subsequent strong signals were concentrated around that point until the final fracture

were concentrated around that point until the final fracture. According to a previous study [11–13] and the observations described below (Figs. 9, 10), the AE event at ~700 s is correlated with the formation of the maincrack, which grows to the final fracture. The critical loads for maincrack formation, P_C, and final fracture, P_B, were then determined as shown in Fig. 7a. Ultimately, it was demonstrated that modified apparatus can be used for the online monitoring of microdamage in ceramic femoral heads with the AE technique.

Twenty specimens were examined in this study. P_C and P_B were examined statistically based on Weibull's statistics [17]. Figure 8 shows the Weibull plots of P_C and P_B. The average values of P_C and P_B were 2.9 and 6.3 kN, respectively. The Weibull modulus m in P_C was smaller than that in P_B, indicating that P_C has larger variation.

Maincrack observation

To confirm that the maincrack formed when there was a rapid increase in the AE energy in the alumina femoral head, the fracture surface was observed in the following manner (Fig. 9).

1. Before testing, red dye (R-1A NT, Eishin Kagaku Co.) was applied to the surface of the tapered bore and urethane rubber.

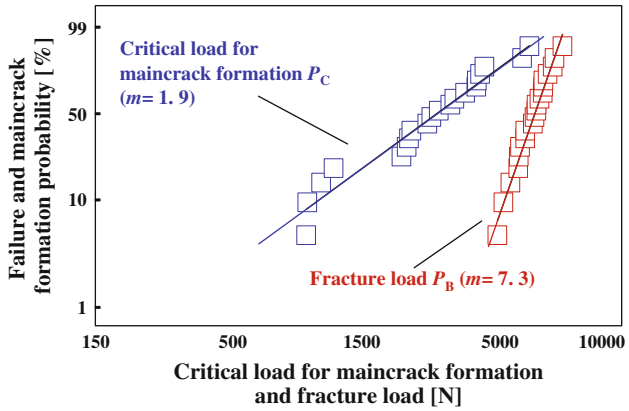

Fig. 8 Weibull plot of the applied load. The average values of P_C and P_B were 2.9 and 6.3 kN, respectively. P_C has greater variation than P_B

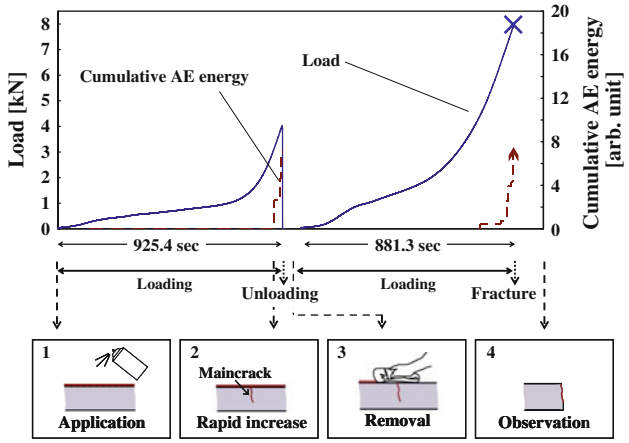

Fig. 9 Schematic illustration of the sequence for dye penetrant observation of maincrack formation: *1* red dye was applied to the surface of the tapered bore and urethane, *2* once the rapid increase in AE energy was detected, the applied load was removed immediately, *3* the dye on the surface was removed completely, and *4* the fracture surface was observed with an optical microscope after loading to fracture again (Color figure online)

2. A mechanical load was applied to the specimen. Once the rapid increase in AE energy was detected, the applied load was removed immediately.
3. The dye on the surfaces was removed completely.
4. The specimen was loaded again to fracture and the fracture surface was observed with an optical microscope.

Figure 10 shows the fracture surface. A spot with red penetration was found at the center of the hackle pattern on the fracture surface, suggesting that the maincrack formed at the rapid increase in AE energy. Thus, the formation of the maincrack during the compression test of the femoral head can be detected with the AE technique, similarly to the bending tests. Finally, it was verified that the

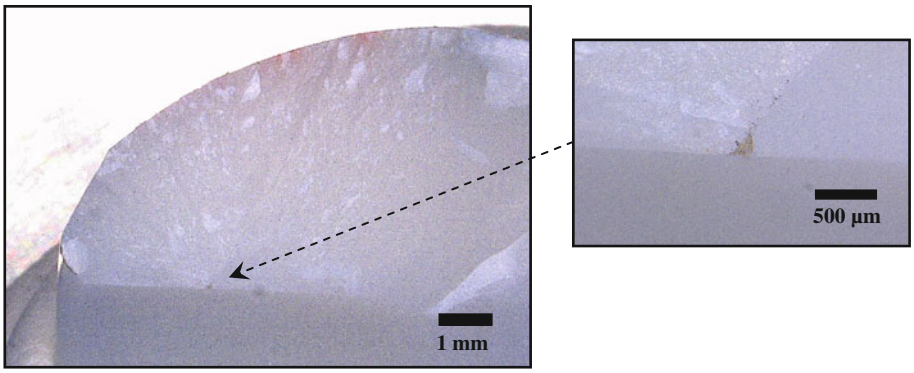

Fig. 10 Micrograph of the fracture surface. A spot with penetration can be seen at the center of the hackle pattern, suggesting that the maincrack formed at the rapid increase in the cumulative AE energy

microfracture process of a ceramic femoral head consisted of maincrack formation, due to microdamage accumulation, followed by its growth to the final fracture.

Discussion

Finite element analysis of the stress distribution in a femoral head

The applied load measured above is unique for the modified configuration developed in this study. Thus, for general discussion, the stress distribution in a ceramic femoral head was computed using commercial FEM code (ANSYS 12.0).

A two-dimensional (2D) axisymmetric model was constructed for the analysis (Fig. 11). The numbers of elements and nodes are tabulated in Table 2. The model consisted of 2D 8-node structural solid, with quadrilateral-shaped elements. The element types and mechanical properties of each component are also shown in Table 3. The Young's modulus, E, and Poisson's ratio, ν, of the tapered rod are those of the steel used in this study. The supporting copper ring was fixed and assumed to be a rigid body. The material property of the segments was selected as orthotropic and the Young's modulus in the theta (circumferential) direction was an infinitesimal value ($=10^{-5}$ Pa) to simulate the motion of the divided segments. The mechanical properties of the urethane rubber were defined using the Mooney-Rivlin model. The strain energy density function of the model is expressed as:

$$W = C_{10}(I_1 - 3) + C_{01}(I_2 - 3) + C_{11}(I_1 - 3)(I_2 - 3) \quad (1)$$

where C_{10}, C_{01}, and C_{11} are material constants and I_1 and I_2 are strain invariants. The three material constants were determined by curve-fitting the experimental results of a uniaxial compression test of the urethane rubber used in the modified apparatus. Figure 12 shows the stress–strain curve from the experiment and fitting curve. The

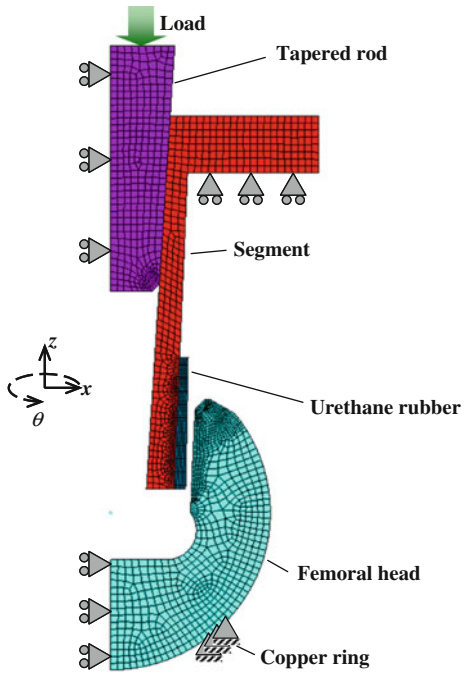

Fig. 11 Schematic illustration of the boundary conditions and meshed elements. A 2D axisymmetric model was constructed for the analysis. The copper ring was assumed to be a rigid body

Table 2 Numbers of elements and nodes for each component

Components	Number of elements	Number of nodes
Tapered rod	1001	3185
Segments	348	1141
Femoral head	738	2210
Urethane rubber	557	1526
Total	2644	8062

experimental and fitted data show good agreement with each other. The resulting values of C_{10}, C_{01}, and C_{11} are included in Table 3. The coefficients of friction in the model are determined as shown in Table 4, so that the calculated strain behavior was consistent with the experimental results.

Table 3 Element types and mechanical properties for each component

Components	Material	Element type	Mechanical property
Tapered rod	SUS630 H900	Isotropic elastic model	$E = 212$ GPa
			$v = 0.27$
Segments	SUS630 H900	Orthotropic elastic model	E_x, $E_z = 212$ GPa
			$E_\theta = 10^{-5}$ Pa
			$v_\theta = 0.27$
Femoral head	Alumina (Al_2O_3)	Isotropic elastic model	$E = 400$ GPa
			$v = 0.24$
Urethane rubber	Urethane	Superelastic Mooney–Rivlin model	$C_{10} = 15.428$ MPa
			$C_{01} = -9.193$ MPa
			$C_{11} = 1.495$ MPa

The element type and mechanical properties of the segments were chosen to be an orthotropic elastic material to simulate the motion of the divided segments. Urethane rubber was defined using the Mooney–Rivlin model, and the parameters C_{10}, C_{01}, and C_{11} were determined by curve fitting with the experimental results of the uniaxial compression test (Fig. 12)

Table 4 The coefficients of friction in the model. These were determined so that the calculated strain behavior was consistent with the experimental results

	Coefficient of friction
Femoral head/copper ring	0.01
Loading rod/divided segments	0
Urethane rubber/femoral head	0.3

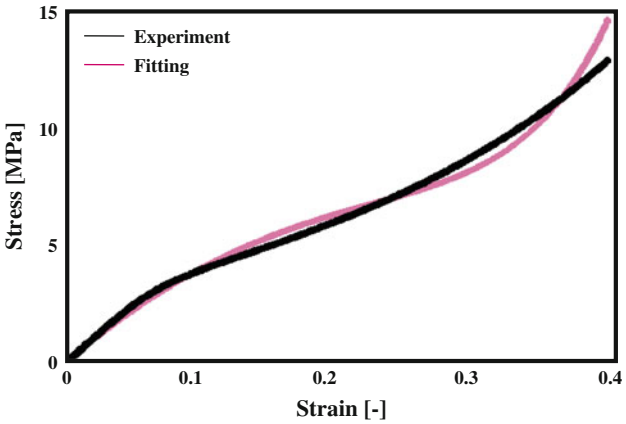

Fig. 12 Stress–strain curve from the experimental results of a uniaxial compression test of urethane rubber used for the modified compression test and fitting curve. They show good agreement with each other. The resulting values of C_{10}, C_{01}, and C_{11} are included in Table 3

Figure 13 describes the strain distributions obtained from the FEA and experiments. The figure compares the computed and experimentally measured strains at the mouth of the bore and great circle, and these show good agreement with each other. The right figure shows the entire strain distribution in the circumferential direction just before the final fracture. As the figure shows, the mouth of the bore is subjected to the maximum strain.

The circumferential stress along the path on the inner surface of the bore of the femoral head was investigated to verify the numerical analysis. The stress distributions at corresponding loads, P, are shown in Fig. 14. The maximum stresses were observed around the mouth of bore (range between points B to C) at any applied load. Considering the equivalence of the circumferential stress to the first principal stress, the stress distribution obtained is consistent with the fact that the fracture origins of most specimens were found around the mouth of bore. Consequently, it can be concluded that the constructed model is adequate for discussing the stress distribution in a ceramic femoral head.

Statistical aspects of strength of femoral head

Using the model described above, the critical stress for maincrack formation, σ_C, and the fracture strength, σ_B, obtained from the results of compression tests of ceramic femoral heads were examined. Figure 15 shows the Weibull plots for σ_C and σ_B. In the figure, σ_C and σ_B are determined as the maximum first principal stress in the specimen at the load corresponding to the rapid increase in AE energy (P_C in Fig. 8) and the final fracture (P_B in Fig. 8), respectively. The average σ_C was 182 MPa and the average σ_B was 384 MPa. It is worth noting that the specimen with low σ_C does not always have low σ_B, i.e., σ_C and σ_B are independent of each other. This may be because the critical condition for final fracture is dominated by the transition from stable to unstable crack growth, while that for maincrack formation may be the coalescence of microcracks.

It is recognized in Fig. 15 that four plots of σ_C are separated from the others. The fracture origins of a few

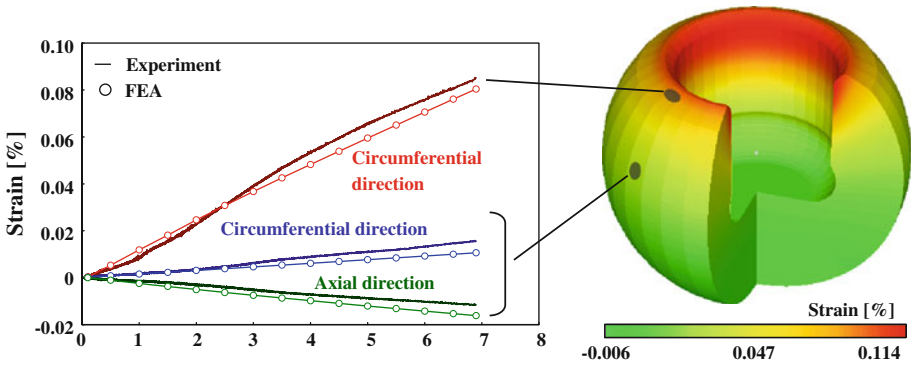

Fig. 13 Comparison of the strain distributions obtained from the FEA and experiments. The computed and measured strains show good agreement with each other. The map on the right describes the circumferential strain distribution just before the final fracture

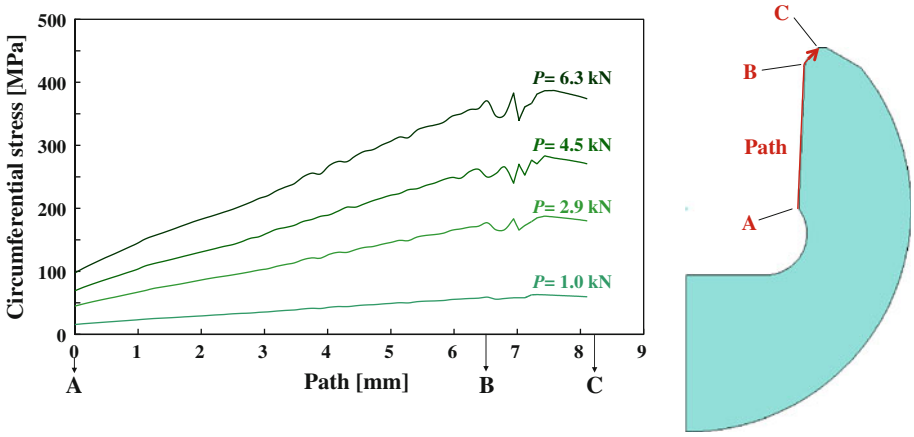

Fig. 14 Stress distributions along the inner surface of the bore at the corresponding loads. $P = 6.3$ and 2.9 kN are the values for the average loads for fracture and maincrack formation, respectively. Locations A, B, and C are indicated in the right figure

specimens were found near the bore surface farther than 4 mm from the mouth of the bore. Thus, the critical stress for maincrack formation, σ_C, and the fracture strength, σ_B, were determined in another way, i.e., the first principal stress at the fracture origin. The Weibull plots of those values of σ_C and σ_B are presented in Fig. 16. The figure shows that the plots of both σ_C and σ_B are arranged continuously. The average σ_C and σ_B were 156 and 334 MPa, respectively, and the shape parameters were lower than those obtained in Fig. 15 because the stress decreases with the distance from the mouth of the bore.

On the other hand, the average strength in the four-point bending test using parallelepiped specimens ($3 \times 4 \times 40$ mm) of the same material was 238 and 501 MPa for σ_C and σ_B, respectively [13]. The average strengths in compression tests of the femoral head were smaller than in the bending tests. This may be attributed to the size effect of strength, a well-known feature of brittle materials. The difference in stress states may be another factor.

The load applied during the compression tests was reduced markedly by the modification of the apparatus. Consequently, the critical loads for maincrack formation, P_C, and for final fracture, P_B, are unavailable for practical use, because the design and utilization of femoral heads are usually based on data using the conventional apparatus [18]. Thus, the analysis and calculated stress are

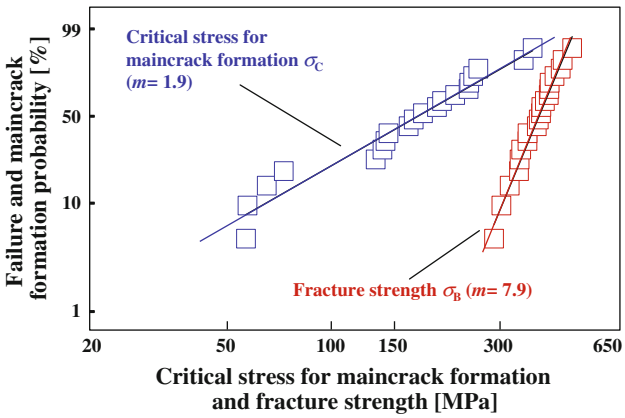

Fig. 15 Weibull plots of σ_C and σ_B. These values were determined as the maximum principal stress at the loads corresponding to the rapid increase in AE energy and the fracture loads. The average σ_C was 182 MPa and the average σ_B was 384 MPa

indispensable for establishing a method to assess the reliability, such as proof testing of ceramic femoral heads.

Conclusions

In this study, the authors conducted compression tests of the alumina femoral heads used in hip arthroplasty and

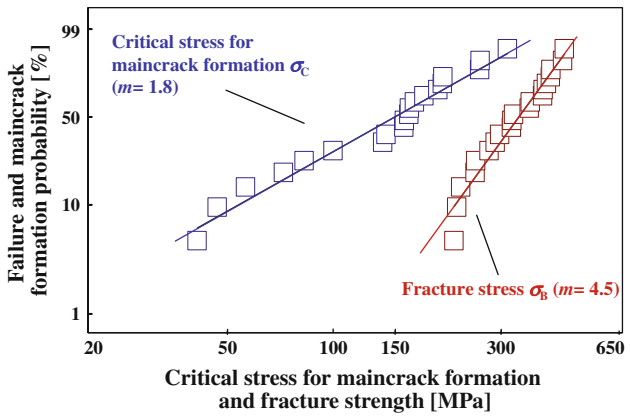

Fig. 16 Weibull plots of σ_C and σ_B. These values were determined as the first principal stress at the fracture origin. The mean values of σ_C and σ_B were 156 and 334 MPa, respectively

characterized the microfracture process based on AE monitoring of the microdamage. To enable an AE detection of microcracks, a modified testing apparatus was developed. Furthermore, the stress and strain distributions were analyzed using finite element analysis (FEA). The following conclusions were obtained.

(1) The test apparatus used for compression tests of the alumina femoral heads used in hip arthroplasty was modified. The strain distribution in the specimen was equivalent to that with the conventional apparatus standardized in ISO 7206. The friction between the loading rod and specimen was restrained, so that AE monitoring of the microdamage was enabled.

(2) Microdamage accumulation in ceramic femoral heads during compression testing was identified using an AE technique. The microfracture process consists of the maincrack formation due to the accumulation of microdamage, and its growth to the final fracture. It was similar to the previous result in bending tests.

(3) The stress distribution during the test was computed using FEA, and the critical stresses for maincrack formation and fracture strength were determined. These values were smaller than those found in the four-point bending test. This may result from the size effect of strength and the difference in the stress state.

The critical stress for maincrack formation may be more conservative parameter than the final fracture strength. In addition, because it is considered by the analogy with fatigue lifetime of metals that the time-to-maincrack formation is dominant in the lifetime of bioceramics, the critical stress σ_C can be used as a measure of the design parameter. This study developed an experimental technique for detecting microdamage in ceramic femoral heads during the compression test. It will enable the AE monitoring of microdamage during proof testing of ceramic femoral heads. Finally, this study provided fundamental insights into the reliability assessment of ceramic femoral heads.

References

1. Hench LL (1993) Bioceramics. J Amer Ceram Soc 81:1705
2. Hench LL, Wilson J (1993) An introduction to bioceramics. World Scientific, Singapore
3. Clarke IC et al (2003) J Bone Joint Surg 85-A:73
4. Evans AG (1972) J Mater Sci 7:1137. doi:10.1007/BF00550196
5. Evans AG, Linzer M (1973) J Amer Ceram Soc 56:575
6. Davidge RW, McLaren JR, Tappin G (1973) J Mater Sci 8:1699. doi:10.1007/BF02403519
7. Evans AG, Wiederhorn SM (1974) Int Jour Fracture 10:379
8. Ritter JE Jr, Oates PB, Fuller ER Jr, Wiederhorn SM (1980) J Mater Sci 15:2275. doi:10.1007/BF00552317
9. Fuller ER Jr, Wiederhorn SM, Ritter JE Jr, Oates PB Jr, Wiederhorn SM, Ritter JE Jr, Oates PB (1980) J Mater Sci 15:2282. doi:10.1007/BF00552318
10. Weisse B, Affolter C, Koller RE, Stutz A (2010) Proc IMechE Part H 224:1051
11. Wakayama S, Koji T, Nishimura H (1991) Trans Jap Soc Mech Eng 57:504
12. Wakayama S, Nishimura H (1992) In: Fracture mechanics of ceramics, vol 10. Plenum Publishing Co., New York
13. Wakayama S, Ikeda C, Ikeda J (2006) J Acoustic Emission 24:228
14. ISO-7206-10, Implants for surgery—Partial and total hip-joint prosthesis—Part 10: determination of resistance to static load of modular femoral head
15. Wakayama S, Horide A, Kawahara M (1999) In: Proceedings of the 12th International conference on composite materials (CD-ROM), Paris
16. Horide A, Wakayama S, Kawahara M (1999) Adv Compos Mater 8:139
17. Weibull W (1951) J Appl Mech 18:293
18. FDA Guidance (draft), Guidance Document for the Preparation of Premarket Notification for Ceramic Ball Hip System